MIT Open Access Articles

Prediction and Characterization of Dry-out Heat Flux in Micropillar Wick Structures

Prediction and Characterization of Dry-out Heat Flux in Micropillar Wick Structures

Yangying Zhu[1], Dion S. Antao[1], Zhengmao Lu[1], Sivanand Somasundaram[2], Tiejun Zhang[3], Evelyn N. Wang[1,]*

[1] Department of Mechanical Engineering, Massachusetts Institute of Technology, Cambridge, MA 02139, USA

[2] Singapore-MIT Alliance for Research and Technology (SMART) Centre, LEES, 1 CREATE way, 138602, Singapore

[3] Department of Mechanical and Materials Engineering, Masdar Institute of Science and Technology, P.O. Box 54224, Abu Dhabi, UAE

ABSTRACT: Thin-film evaporation in wick structures for cooling high performance electronic devices is attractive because it harnesses the latent heat of vaporization and does not require external pumping. However, optimizing the wick structures to increase the dry-out heat flux is challenging due to the complexities in modeling the liquid-vapor interface and the flow through the wick structures. In this work, we developed a model for thin-film evaporation from

micropillar array wick structures and validated the model with experiments. The model numerically simulates liquid velocity, pressure, and meniscus curvature along the wicking direction by conservation of mass, momentum and energy based on a finite volume approach. Specifically, the three-dimensional meniscus shape, which varies along the wicking direction with the local liquid pressure, is accurately captured by a force balance using the Young-Laplace equation. The dry-out condition is determined when the minimum contact angle on the pillar surface reaches the receding contact angle as the applied heat flux increases. With this model, we predict the dry-out heat flux on various micropillar structure geometries (diameter, pitch and height) in the length scale range of 1-100 μm and discuss the optimal geometries to maximize the dry-out heat flux. We also performed detailed experiments to validate the model predictions, which show good agreement. This work provides insights into the role of surface structures in thin-film evaporation and offers important design guidelines for enhanced thermal management of high-performance electronic devices.

1. INTRODUCTION

The increasing power densities in high performance electronic devices such as GaN power amplifiers, concentrated photovoltaics and laser diodes pose a significant thermal management challenge[1–3]. The use of the liquid-to-vapor phase-change process to cool these devices is attractive because it harnesses the latent heat of vaporization with minimal temperature rise[4–6]. In particular, capillary-pumped thin-film evaporation has gained increasing attention due to its simple design, stable and self-regulating performance, and minimal pumping power consumption[7–9]. These systems generally require a porous wick structure to generate capillary pressure which drives the liquid flow as it evaporates. Among various wick structures

investigated including spheres, pyramids and cylindrical micropillars, the latter have been shown to be a particularly effective wick structure[10]. However, optimizing the micropillars to increase the dry-out heat flux, which is the maximum heat flux the system can dissipate before dry-out occurs, is challenging owing to the complex liquid-vapor interface and its effect on the liquid transport. Thus, existing models simplify the physics by assuming an adiabatic flow[11,12], or neglecting the variation of the three-dimensional curved liquid-vapor interface[13–15] along the length of the wick. In addition, these models are typically based on the Brinkman's equation[11,12,16] or Darcy's law[14,15] which describes flow in an isotropic porous media, with an effective porosity and permeability adopted for the micropillars. Therefore, a multi-physics model, which captures the liquid-vapor interface along the wicking distance and couples the associated capillary pressure field with the fluid and enthalpy transport, is needed for more accurate predictions of the dry-out heat flux.

In this study, we developed a numerical model for thin-film evaporation from micropillar array wick structures. The model simulates the liquid velocity, pressure, and meniscus curvature along the wicking direction by conservation of mass, momentum and energy based on a finite volume approach. In particular, the three-dimensional meniscus shape, which varies along the wicking direction with the local liquid pressure, is accurately captured by the Young-Laplace equation. We determine the dry-out condition at a fixed distance from the liquid source when the minimum contact angle on the pillar surface reaches the receding contact angle as the applied heat flux is increased. We predict the dry-out heat flux on various micropillar structure geometries (diameter *d*, pitch *l*, and height *h*) in the length scale range of 1-100 μm and suggest the optimal geometries to maximize the dry-out heat flux. In addition, we experimentally validated the model with microfabricated test samples and measured the heat flux at which dry-out occurred. The results

show that for the geometric range investigated, the dry-out heat flux is maximized at $d/h \sim 0.4$-0.6 and $l/d \sim 3$.

2. MODEL FORMULATION

In this work, we study capillary-pumped liquid film evaporation on a hydrophilic micropillar array surface (or the "wick surface") of length L, in a constant pressure, saturated vapor environment. A schematic of the problem studied in this model is shown in Figure 1a (side view) and 1b (top view). Figure 1c shows a scanning electron microscope (SEM) image of a representative fabricated silicon micropillar array with diameter of d, pitch of l and height of h (d, h, $l << L$). The wick surface in Figure 1a and 1b ($0 \le x \le L$) is in contact with a liquid reservoir ($x < 0$) at $x = 0$, whose volume is much larger than the total volume of liquid on the wick surface. The wick surface and the liquid in the reservoir are in a saturated environment, with saturated vapor on top. Thus, the pressure of the liquid reservoir (flat interface) is the same as the vapor pressure P_{vap}, which is constant (at P_{sat}) in this system. Upon applying a uniform heat flux q to the bottom of the wick surface, the liquid film evaporates and the film thickness reduces as a function of x. The bottom surface is assumed to be infinitesimally thin such that no axial conduction is present in the solid, which can be large for a thick substrate[17]. However, the liquid-vapor interface is pinned to the hydrophilic micropillar top surfaces. As a result, concave interfaces form (shown in Figure 1a). After the system evolves to equilibrium, the curvature $\kappa(x)$ of this interface increases with x, which is a result of a thinner liquid film further from the reservoir. The liquid pressure $P_{liq}(x)$ is described by the Young-Laplace equation,

$$P_{vap} - P_{liq}(x) = 2\sigma\kappa(x) \tag{1}$$

where σ is the liquid-vapor surface tension. For the geometries (1-100 μm) and evaporation conditions studied in this model, the variations of the surface tension with temperature, the disjoining pressure and recoil pressure are negligible. The liquid pressure gradient along x, dP_{liq}/dx, thus results in a net flow from the reservoir (marked by the blue solid arrow in Figure 1a), which compensates for the evaporated liquid mass flux. The goal of this modeling study is to understand the axial variation of the pressure $P(x)$ and the x-direction liquid velocity $U(x)$ at any heat flux q. With this information, we determined the dry-out heat flux $q_{dry\text{-}out}$, as the meniscus curvature at $x = L$ reaches its maximum (*i.e.*, where the liquid-vapor meniscus starts to recede).
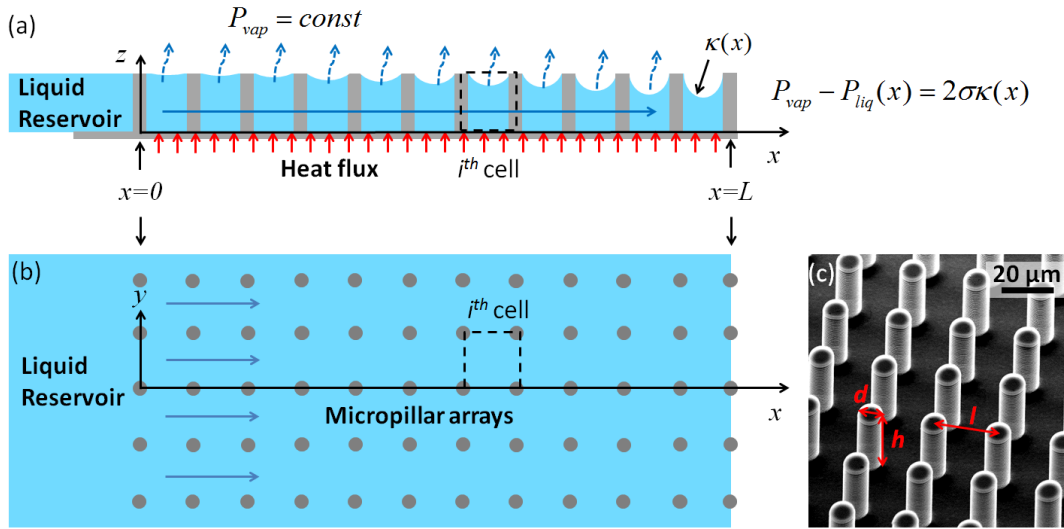
Figure 1. (a) Side view and (b) top view schematics of the physical domain in this model. Capillary-pumped liquid film evaporates on a hydrophilic micropillar array surface of length L, where a uniform heat flux is applied. The vapor pressure P_{vap} is constant. The Young-Laplace equation is given, where σ is the liquid-vapor surface tension and $\kappa(x)$ is the curvature of the liquid-vapor interface at any x. (c) A representative SEM image of a fabricated silicon micropillar array with diameter d, pitch l and height h.

Since the micropillars are periodic with pitches of *l*, we divide the liquid domain into finite volumes or unit cells. Each unit cell is the fluid volume within four pillars shown in the dotted box in Figure 1a and 1b. Since the flow pattern is identical for any finite volume with the same *x* (*i.e.,* the system is periodic in the *y* direction), we only consider one row of unit cells. We first consider the meniscus shape in one unit cell from the Young-Laplace equation, and solve for the velocity field in one unit cell using a CFD model. We then link all of the cells from $x = 0$ to $x = L$ based on a finite volume approach where we analyze the change of liquid enthalpy and mass flow rate across a finite volume, and match the mass flux and enthalpy flux for adjacent cells.

A. Force Balance. We first solve for the meniscus shape at an arbitrary unit cell along *x* with the liquid pressure $P_{liq}(x)$. The curvature of the meniscus in one unit cell is governed by the Young-Laplace equation (equation (1)). Since P_{vap} is constant, we define $P_{r,liq}$ as the liquid pressure relative to the vapor pressure, $P_{r,liq} = P_{liq} - P_{vap}$. In the scenarios of practical interest, *L* is usually much greater than *l*. It is therefore reasonable to assume that the pressure and curvature variations in one unit cell are small, which we will later validate. Under this condition ($L>>l$), the meniscus in the ith cell which is governed by $\kappa(x)$ or $P_{r,liq}(x)$ is approximated using the meniscus calculated from a cell-averaged curvature κ^i (or the cell-averaged pressure $P_{r,liq}{}^i$), since in this numerical model we discretize the pressure $P_{r,liq}(x)$ as $P_{r,liq}{}^i$ (*i*=0 to *L*/*l*). Accordingly, we denote *x'*, *y'* and *z'* as the relative coordinates in a unit cell. Equation (1) is then rearranged to equation (2).

$$\kappa^i = \frac{-P_{r,liq}{}^i}{2\sigma} \tag{2}$$

The curvature of a 3-D surface $z' = f(x',y')$ is calculated as,

$$2\kappa^i = -\nabla \cdot \hat{n} \tag{3}$$

where $\hat{n}$ is the unit normal of the surface defined as equation (4)[18].

$$\hat{n} = \frac{(\frac{\partial f}{\partial x'}, \frac{\partial f}{\partial y'}, -1)}{\left[\left(\frac{\partial f}{\partial x'}\right)^2 + \left(\frac{\partial f}{\partial y'}\right)^2 + 1\right]^{1/2}}$$

(4)

Given any $P_{r,liq}{}^i$, the constant-mean-curvature (CMC) meniscus shape $z' = f_{meniscus}(x',y')$ is numerically computed using equation (3) and (4) in COMSOL[19] by setting $\kappa^i = -P_{r,liq}{}^i/(2\sigma)$.

The boundary conditions (before the meniscus starts to recede within the unit cell) are: a) the interface is pinned at the pillar top,

$$z' = h \text{ at } \begin{aligned} x'^2 + y'^2 &= (d/2)^2, \\ (x'-l)^2 + y'^2 &= (d/2)^2, \\ x'^2 + (y'-l)^2 &= (d/2)^2, \\ (x'-l)^2 + (y'-l)^2 &= (d/2)^2, \\ 0 \leq x', y' &\leq l \end{aligned}$$

(5)

and b) the slope of the meniscus where adjacent cells meet is continuous. More specifically, the slope in the x' direction should be zero at $x' = 0$ and l, when the pressure difference between adjacent cells is infinitesimally small, and the slope in the y' direction is zero at $y' = 0$ and l, due to symmetry.

$$\frac{\partial z'}{\partial x'} = 0 \text{ at } x' = 0, l \text{ and } \frac{\partial z'}{\partial y'} = 0 \text{ at } y' = 0, l$$

(6)

Due to the various geometries simulated (1-100 μm), we used a standard optimized mesh generation algorithm in COMSOL[19] to generate the grid. The minimum and maximum relative mesh areas (with respect to the unit cell projected area) were approximately 1×10^{-5} and 7×10^{-5}.

The relative tolerance for the convergence of z' was 10^{-6}. The results were exported in the form of points (x', y', z').

An example of the meniscus in a unit cell (d=3 μm, l=9 μm, h=5 μm) with $\kappa^i = 5.52 \times 10^{-2}$ μm^{-1} which corresponds to $P_{r,liq} = -6.49$ kPa ($\sigma = 58.8$ mN/m, water at 100 ℃) is shown in Figure 2a. We choose water due to its large latent heat of vaporization compared to other fluids. From the meniscus solution, we further obtain the contact angle θ that the meniscus makes on the pillar surface. The contact angle varies around the pillar circumference ($29.92° < \theta < 30.21°$) as expected due to the non-axisymmetric geometry and interactions with the adjacent three pillars (see Supporting Information Sections S-I and S-II), but this variation is small for pillar geometries with reasonably large permeability which is of practical interest in wicking applications. In this case, the corresponding average contact angle obtained from the meniscus solution around a pillar is $\theta = 30.06°$, which matches very well with the average contact angle ($\theta = 30.00°$) calculated from a force balance analysis (see Supporting Information Section S-I for detail) described by equation (7),

$$\sigma(\pi d)\cos\theta = -P_{r,liq}(l^2 - \pi r^2) \tag{7}$$

where r ($r = d/2$) is the radius of the pillar. The left hand side of equation (7) represents the vertical component of the line forces pulling the meniscus upward (indicated by red arrows in Figure 2a). The right hand side of equation (7) is the downward component of the force from the pressure difference acting on the meniscus.
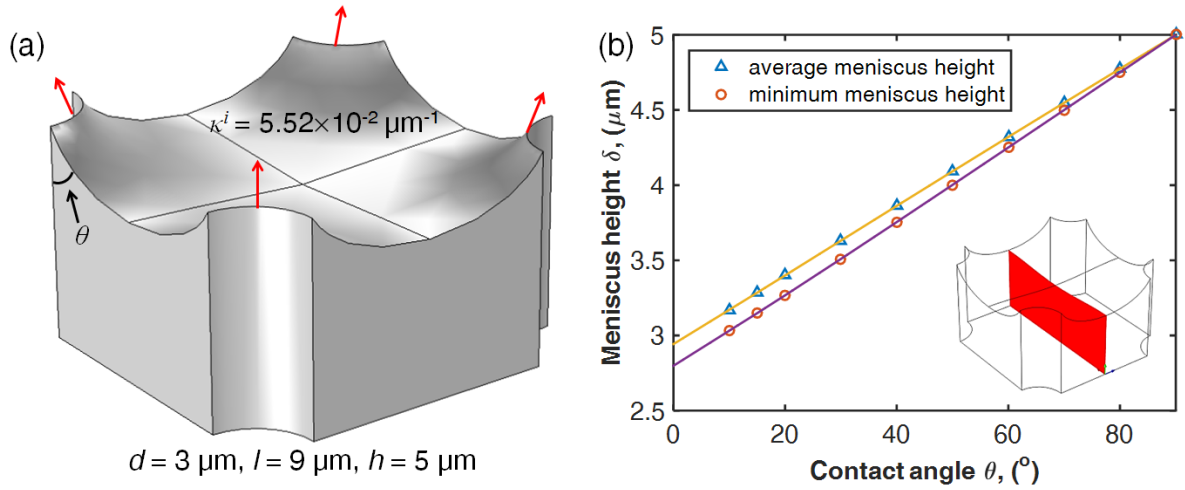
Figure 2. (a) The meniscus shape for $d = 3$ μm, $l = 9$ μm, $h = 5$ μm and $\kappa^i = 5.52 \times 10^{-2}$ μm^{-1}, computed from equation (3) and (4) in COMSOL. The corresponding average contact angle for this meniscus shape is $\theta = 30.06°$. (b) The average meniscus height and minimum meniscus height in the center yz-plane (the red plane in the inset) of a unit cell ($d = 3$ μm, $l = 9$ μm, $h = 5$ μm) as a function of the average contact angle θ around the pillars. The solid lines are linear interpolation and extrapolation of the data points from COMSOL.

Figure 2b shows an example of the average meniscus height and minimum meniscus height of the center yz-plane in a unit cell (the red plane in the inset of Figure 2b) as a function of the contact angle θ ($d=3$ μm, $l=9$ μm, $h=5$ μm), or curvature κ. The result shows that, for this particular pillar geometry, the liquid-vapor interface curves towards the bottom surface for ~40% the total height of the pillar at small contact angles. This indicates that assuming the liquid thickness is equal to the micropillar height can largely underpredict the flow resistance, especially for small h/l ratio geometries. Following the same method, we solved the meniscus shape for various pillar geometries and $P_{r,liq}$ (or κ) using a parametric sweep in COMSOL.

B. Momentum Equation. We next solve the momentum equation (Navier-Stokes Equations) for the velocity field (u,v,w) in one unit cell as a function of the relative liquid pressure $P_{r,liq}$ which determines the meniscus shape, and the pressure difference across one unit cell $\Delta P_{r,liq}/l$ which drives the flow. Due to the complexity of the meniscus shape, we solve the three-dimensional velocity profile $(u,v,w) = f(P_{r,liq}, \Delta P_{r,liq}/l, x', y', z',$ micropillar geometries) numerically *via* CFD simulations in COMSOL. We imported the meniscus shape (x', y', z') calculated in Section 2A *via* parametric surface in COMSOL as a geometric boundary. We choose the fluid properties of water at 100 ℃. Figure 3a shows an example of a unit cell ($d = 3$ μm, $l = 9$ μm, $h = 5$ μm). For any input $P_{r,liq}$, the meniscus is first generated by the method described in Section A. A pressure difference $\Delta P_{r,liq}$ is applied across the inlet and the outlet of the fluid domain, which represents a cell-averaged pressure gradient $dP_{r,liq}/dx \approx \Delta P_{r,liq}/l$. The boundary conditions are a) no-slip boundary condition on the bottom surface and the pillar side walls, b) shear free boundary condition on the meniscus and c) symmetric boundary condition on the side walls of the unit cell ($y = 0$ plane and $y = l$ plane). The minimum and maximum relative mesh volumes (with respect to the unit cell volume) were approximately 1×10^{-6} and 1.5×10^{-4}. The relative tolerance for the convergence of velocity and pressure was 10^{-3}. The Mesh independence of the numerical solution is included in Supporting Information S-III. Figure 3a shows the result of the magnitude of the velocity (m/s) in the fluid domain where $P_{r,liq} = -6.49$ kPa which corresponds to $\kappa^i = 5.52 \times 10^{-2}$ μm^{-1} or $\theta = 30°$, and a $\Delta P_{r,liq}/l$ of -1.667 Pa/μm ($\Delta P_{r,liq} = -15$ Pa over $l = 9$ μm).
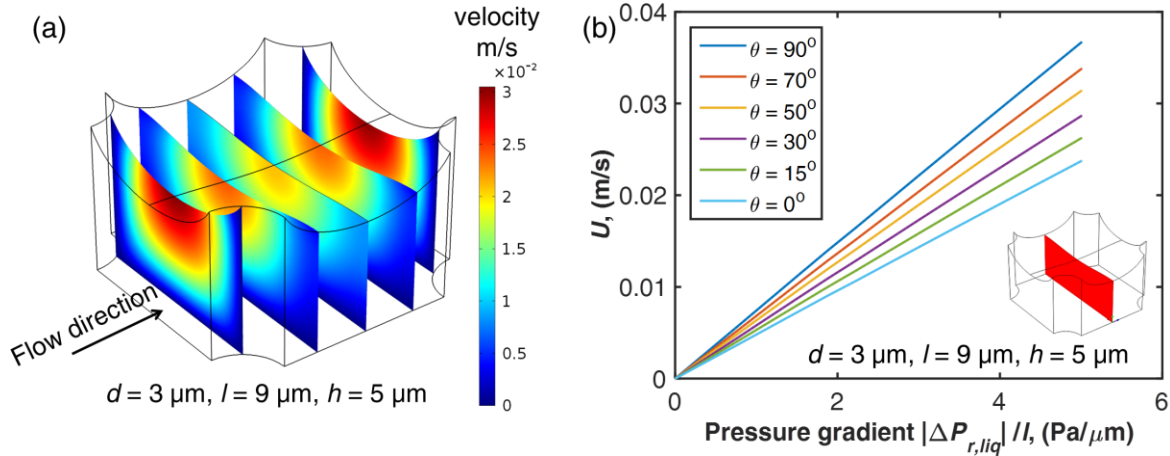
Figure 3. (a) The magnitude of the velocity (m/s) in the fluid domain where $P_{r,liq} = -6.49$ kPa which corresponds to $\kappa^i = 5.52 \times 10^{-2}$ μm^{-1} or $\theta = 30°$, and a $\Delta P_{r,liq}/l$ of -1.667 Pa/μm ($\Delta P = -15$ Pa over $l = 9$ μm). The micropillar geometries are $d = 3$ μm, $l = 9$ μm, $h = 5$ μm. (b) The center-yz-plane-averaged (the red plane in the inset) x-direction velocity U defined as $U = \frac{1}{A_c} \iint_{A_c} u(x', y', z') dy' dz' \big|_{x'=l/2}$ as a function of $|\Delta P_{r,liq}|/l$ and $\theta = f(P_{r,liq})$.

We performed simulations over a wide range of values for pressure gradient $\Delta P_{r,liq}/l$ and pressure $P_{r,liq}$, to obtain their effect on the liquid velocity. The result for $d = 3$ μm, $l = 9$ μm, $h = 5$ μm is plotted in Figure 3b where the center-yz-plane-averaged (the red plane in the inset) x-direction velocity U (defined as $U = \frac{1}{A_c} \iint_{A_c} u(x', y', z') dy' dz' \big|_{x'=l/2}$) is shown as a function of $|\Delta P_{r,liq}|/l$ and $\theta = f(P_{r,liq})$. For a fixed contact angle (*i.e.*, a fixed meniscus shape), the result shows a linear relationship between the velocity and the pressure gradient, which is due to a fixed flow resistance. As θ reduces, the meniscus becomes more concave. This increases the flow resistance, as indicated by the reduced slopes of the U *vs.* $|\Delta P_{r,liq}|/l$ curves. Besides $|\Delta P_{r,liq}|/l$ and pressure $P_{r,liq}$, we also performed simulations over a wide range of sample geometries (d, l, h) to

obtain a look-up table for $U = f(P_{r,liq}, \Delta P_{r,liq}/l, d, l, h)$. We used this look-up table for the finite volume simulations discussed next.

C. Mass Conservation and Enthalpy Balance. We finally connect the unit cells from $x = 0$ to $x = L$ by integrating the mass conservation and enthalpy balance equations in each unit cell, or finite volume, and matching the fluxes at the finite volume interfaces. For the convenience of the study, we chose the finite volumes as shown in Figure 4, so that the boundaries of the finite volumes coincide with the center yz-planes in each unit cell (Figure 4a).
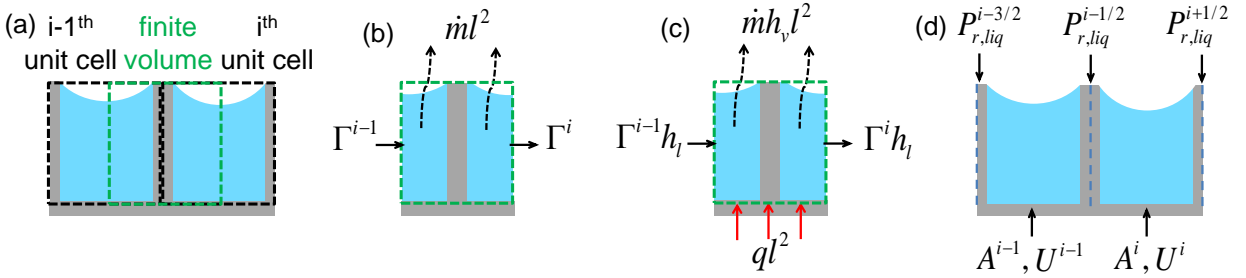
Figure 4. Schematics of (a) the choice of finite volume and unit cells, (b) mass conservation and (c) enthalpy balance on a control volume, and (d) locations of the variables solved in the model.

Integrating the mass conservation in the finite volume gives equation (8),

$$\Gamma^{i-1} - \Gamma^i = \dot{m}l^2 \qquad (8)$$

where Γ^{i-1} and Γ^i represent the mass flow rate entering and leaving the finite volume respectively (Figure 4b), and $\dot{m}$ is the evaporation rate (*i.e.*, the mass evaporated per unit area per second, kg/m^2 s). Γ^i is calculated by integrating the mass flux on the outlet surface and is described by equation (9),

$$\Gamma^i = \rho \iint_{A^i} u\,dy\,dz = \rho A^i U^i \tag{9}$$

where ρ is the liquid density, u is the x-direction velocity, A^i is the outlet surface area which is also the center yz-plane area A_c in a unit cell, and U^i is the surface-averaged velocity (as discussed in Section B). A similar equation is used to calculate Γ^{i-1}.

Integrating the enthalpy in the finite volume gives equation (10),

$$(\Gamma^{i-1} - \Gamma^i)h_l - \dot{m}l^2 h_v + l^2 q = 0 \tag{10}$$

where h_l and h_v are the enthalpies of the liquid and vapor respectively. Substituting equations (8) and (9) into (10), and neglecting the sensible heat results in equation (11),

$$\rho(A^{i-1}U^{i-1} - A^i U^i)h_{fg} = l^2 q \tag{11}$$

where h_{fg} is the latent heat of vaporization (h_v-h_l).

The boundary conditions at $x = 0$ are a) $P_{r,liq} = 0$ since the liquid is in contact with the reservoir, and b) $\Gamma(x = 0) = qlL/h_{fg}$ since all the liquid evaporated from the surface should enter at $x = 0$. Equation (11) links the center-yz-plane-averaged velocity U^i and the area A^i with those in the next unit cell (Figure 4d). Therefore, we solved $P_{r,liq}$ based on a cell-by-cell (forward) approach, since the left boundary conditions ($x = 0$) are specified. Based on the solution from the previous cell ($P_{r,liq}^{i-1/2}$, A^{i-1}, U^{i-1}) whose locations are defined in Figure 4d, $P_{r,liq}^{i+1/2}$ is iteratively solved until $A^i = f(P_{r,liq}^i)$ and $U^i = f(P_{r,liq}^i, (P_{r,liq}^{i+1/2} - P_{r,liq}^{i-1/2})/l)$ satisfies equation (11), where $P_{r,liq}^i$ is the average pressure in the ith cell and $P_{r,liq}^i = 1/2(P_{r,liq}^{i-1/2} + P_{r,liq}^{i+1/2})$. The solution ($P_{r,liq}^{i+1/2}$, A^i, U^i) is then used to calculate ($P_{r,liq}^{i+3/2}$, A^{i+1}, U^{i+1}) in the next cell.

3. RESULTS AND DISCUSSION

In this section, we first show an example of the solution of a micropillar array surface ($d = 10$ μm, $l = 30$ μm, $h = 25$ μm) of length $L = 5$ mm. We choose this characteristic wicking length L based on a 1 cm^2 typical heat dissipation area of electronic devices, where the fluid wicks from the edges to the center. We discuss how we obtain the dry-out heat flux $q_{dry-out}$ based on the minimum contact angle from the solution. We then show the dry-out heat flux $q_{dry-out}$ for various micropillar geometries as the pillar height h increases from 5 μm to 50 μm and discuss the optimal pillar geometries which maximize $q_{dry-out}$. Furthermore, we validate this model with experimental data and demonstrate good agreement between the two. Finally, we show that $q_{dry-out}$ is very sensitive to the wicking length L and is governed by $q_{dry-out} \sim L^{-2}$.

Figure 5 shows the x-direction velocity $U(x)$ (Figure 5a), the relative liquid pressure $P_{r,liq}(x)$ (Figure 5b), the average meniscus height (liquid thickness) in the center yz-plane in each unit cell $\delta(x) = A_c(x)/l$ (Figure 5c), and the average contact angle that the meniscus makes on the micropillar walls $\theta(x)$ (Figure 5d) as a function of the distance x to the reservoir. Three heat fluxes $q = 50$, 60 and 76.1 W/cm^2 were applied and the dashed arrows in Figure 5 indicate the trend as the heat flux increases. The heat flux of 76.1 W/cm^2 corresponds to the dry-out heat flux which will be explained in the following paragraph. Figure 5a shows that the velocity reduces to zero at $x = L$, which is a physical result of total evaporation of the liquid. This also indicates that the error associated with the numerical method is small, since we only specified the left boundary conditions at $x = 0$ and did not set any constraints at $x = L$. Figure 5b shows that $P_{r,liq}$ reduces along the wick surface and the magnitude of the total pressure drop increases with q. In addition, the maximum pressure variation within a unit cell at $q = 76.1$ W/cm^2 is 23.9 Pa (at $x = 0$), which is only 1% of the pressure variation from $x = 0$ to L (−2.17 kPa). This validates our

assumption in section A that the pressure variation in one unit cell is small. Figure 5c and 5d shows that the thickness of the liquid film and the average contact angle reduces along the wick surface. As heat flux increases, the liquid becomes thinner and the contact angle reduces.

We identify the dry-out heat flux $q_{dry\text{-}out}$ by the physical constraint of the minimum contact angle at $x = L$. This contact angle cannot be lower than the receding contact angle θ_r of the fluid on the substrate. Similarly, the receding contact angle has been used to identify the critical heat flux in pool boiling [20,21]. As an example of water on silicon dioxide, which is a common combination, θ_r is approximately 15 °[22]. Thus $q_{dry\text{-}out}$ in this particular case is determined to be 76.1 W/cm², as shown in Figure 5d.
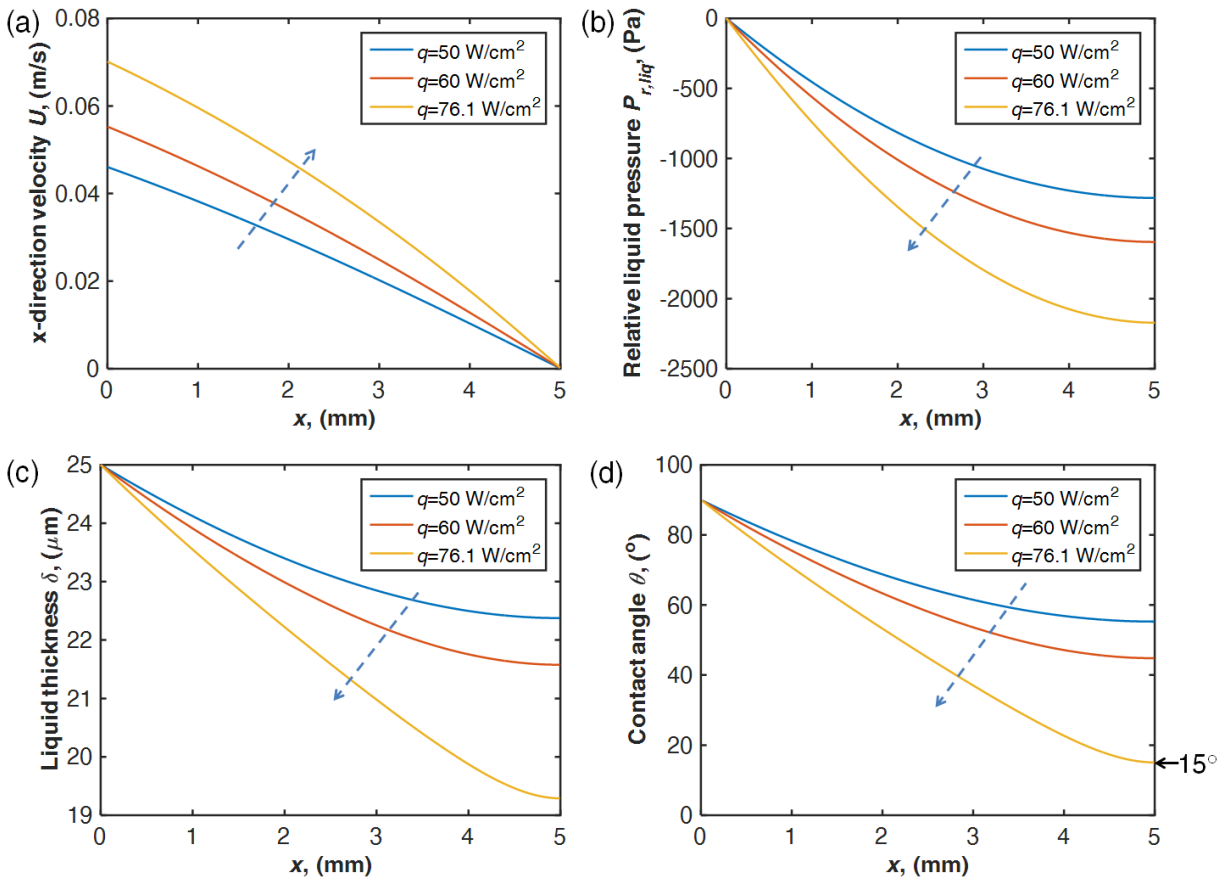
**Figure 5.** A representative set of simulation results for a micropillar array surface ($d = 10$ μm, $l = 30$ μm, $h = 25$ μm) of length $L = 5$ mm at $q = 50$, 60 and 76.1 W/cm². (a) The x-direction

velocity $U(x)$, (b) the relative liquid pressure $P_{r,liq}(x)$, (c) the average meniscus height (liquid thickness) in the center yz-plane in each unit cell $\delta(x) = A_c(x)/l$, and (d) the average contact angle that the meniscus makes on the micropillar walls $\theta(x)$ as a function of the distance x to the reservoir. Water (at 100 ℃) is used as the working fluid.

Following this method, we calculated the dry-out heat flux $q_{dry-out}$ for various micropillar geometries and the results are shown in Figure 6. Micropillars of three different heights ($h = 5$ μm, 25 μm and 50 μm) which correspond to three inlet liquid thickness were investigated. For each h, we examined the micropillar diameters d in the range of approximately $d/h\sim0.1$ to 1. Correspondingly, various micropillar pitches l were considered such that for each d and h, the range of l covers the maximum $q_{dry-out}$. Figures 6a-6c show $q_{dry-out}$ for $h = 5$ μm, 25 μm and 50 μm respectively when $\theta_r = 15°$ (water on silicon dioxide). Figure 6d shows $q_{dry-out}$ for $h = 25$ μm when $\theta_r = 50°$ (representing the case for pillar surfaces with a lower surface energy). The numerical error associated with discretization increases as L/l decreases. Specifically, the number of unit cells becomes less than 50 for $l > 100$ μm ($L = 5$ mm), and the maximum pressure variation within a unit cell at dry-out ($\theta_r = 15°$) for $d = 50$ μm, $l = 100$ μm and $h = 50$ μm increases to 3.6% (40.4 Pa at $x = 0$) of the total pressure variation from $x = 0$ to L (−1.11 kPa).
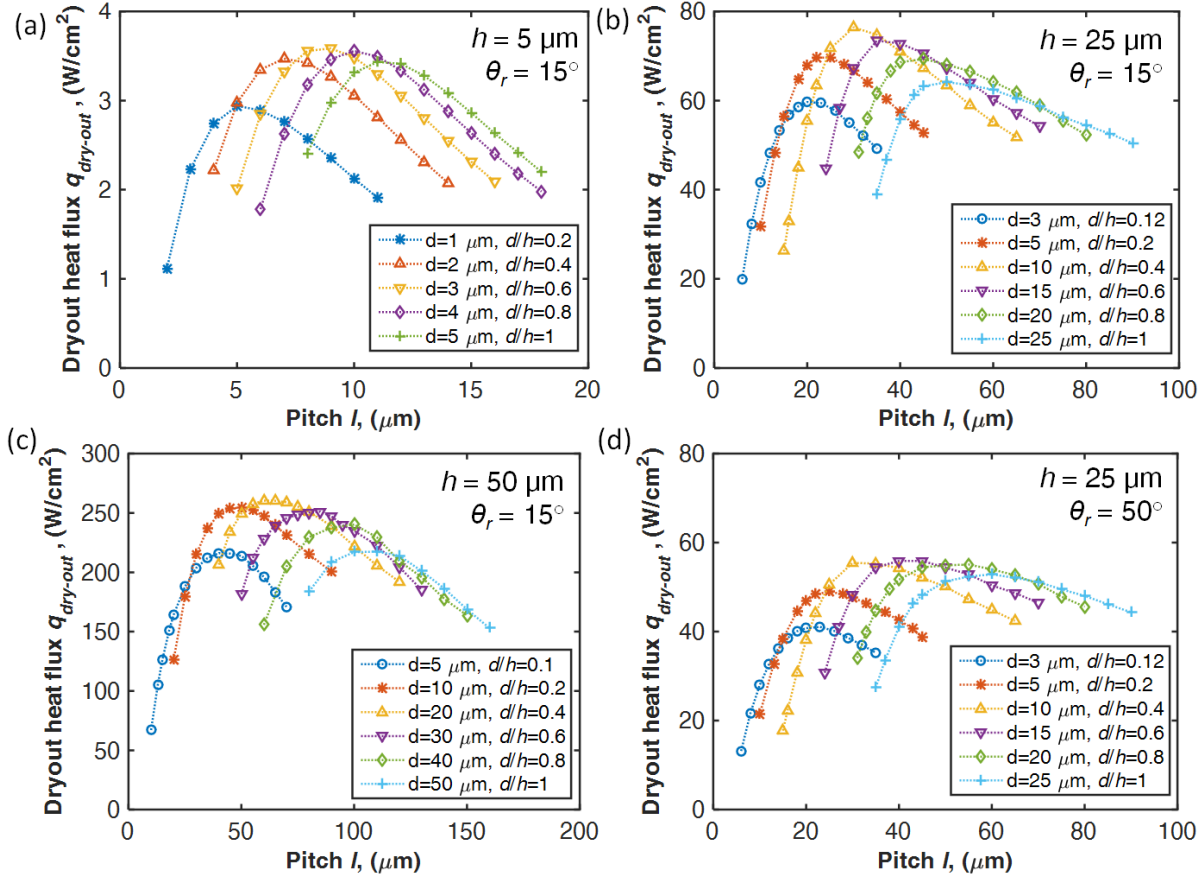
Figure 6. The dry-out heat flux $q_{dry\text{-}out}$ for various micropillar geometries. (a) $h = 5$ μm and $\theta_r = 15°$, (b) $h = 25$ μm and $\theta_r = 15°$, (c) $h = 50$ μm and $\theta_r = 15°$, and (d) $h = 25$ μm and $\theta_r = 50°$.

The results indicate the dry-out heat flux is very sensitive to the choice of the micropillar geometries. We summarize the main observations from these simulations over the parametric space as seen in Figure 6,

(1) For each h, there is a maximum $q_{dry\text{-}out}$, and for the geometries investigated in this study, the optimal geometry has a d/h ratio of approximately 0.4-0.6, and an l/d ratio of approximately 3 when $\theta_r = 15°$.

(2) $q_{dry\text{-}out}$ increases with h (Figure 6a-6c). This is because higher h results in a thicker liquid film and the associated viscus drag ($\sim\mu\,\mathrm{d}u/\mathrm{d}z$) from the bottom surface is smaller. In

17

addition, a thicker liquid allows a higher liquid mass flow rate, which contributes to a higher $q_{dry\text{-}out}$. This trend agrees with previous modeling based on the Darcy's equation and experimental observations [14,15]. However, increasing the height of the pillars increases the superheat at the solid surface. Therefore, h is limited by the maximum superheat associated with the onset of nucleation, which needs further consideration. Due to this boiling limit, we do not report $h > 50$ μm, since a mixed mode of evaporation and boiling has been observed from some previous works [8,23,24] for geometries in this range. Similarly, when the contact angle is large, it is also possible for boiling to occur due to the small evaporative heat transfer coefficient[25].

(3) Reducing θ_r will increase $q_{dry\text{-}out}$, as indicated by Figure 6b and 6d.

To further investigate the effect of the receding contact angle on the dry-out heat flux, we plot $q_{dry\text{-}out}$ as a function of θ_r for three different micropillar geometries (Figure 7). Figure 7 suggests that although the dry-out heat flux increases with decreasing receding contact angle, the increase is small as θ_r approaches 0 °. This relation resembles $q_{dry\text{-}out} \sim \cos\theta_r$ since the maximum capillary pressure is $-P_{r,liq} = \cos\theta_r \sigma(\pi d)/(l^2 - \pi r^2)$, according to equation (7). The exact $q_{dry\text{-}out} = f(\theta_r)$ is micropillar geometry dependent, as indicated by the difference between the curves for $l = 60$ μm and $l = 20$ μm in Figure 7. The predictions for $l = 60$ μm are higher than that for $l = 20$ μm at larger receding contact angles, but becomes lower at receding contact angles less than 21 °. This is because as the contact angle decreases the liquid film becomes thinner for sparse pillar arrays compared to micropillars with relatively closer spacing (insets of Figure 7), which causes more viscous drag. This result explains the trend that the optimal d and l increase as θ_r increases (Figure 6b and 6d). In addition, creating nanoscale hierarchical structures on top of the microscale pillar arrays will not only reduce the apparent contact angle on the pillar surface, but

will also increase the contact line length of the meniscus. This can potentially increase the maximum allowable capillary pressure significantly without introducing substantial viscous loss, which can potentially further increase the dry-out heat flux.
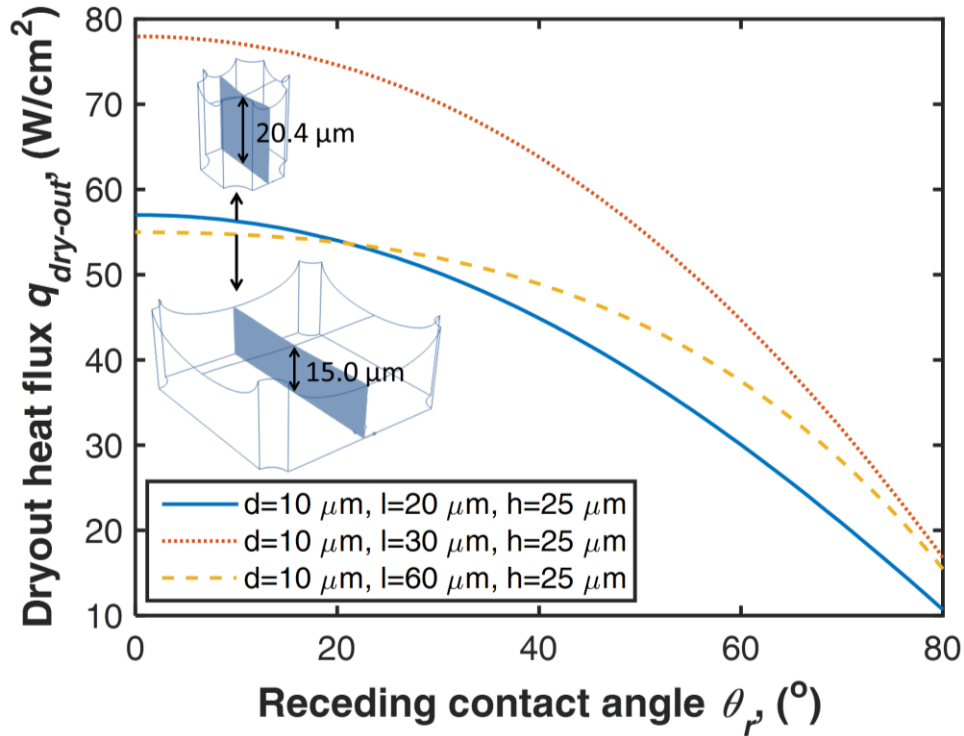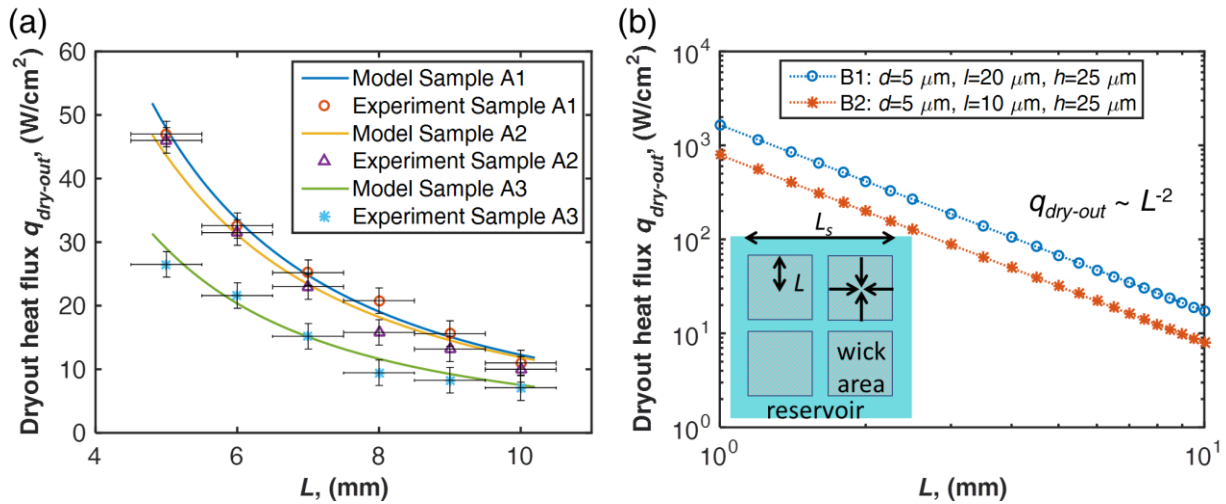

Figure 7. The dry-out heat flux as a function of the receding contact angle for three different micropillar geometries. The dry-out heat flux increases as the receding contact angle decreases. The insets show the minimum liquid film thicknesses for a sparse and dense pillar arrays ($h =$ 25 μm) with $\theta_r = 10$ °.

Furthermore, we validated our model with experimental data. We created well-defined micropillar arrays with three geometries (Sample A1: $d = 7$ μm, $l = 20$ μm, $h = 20$ μm, A2: $d = 7$ μm, $l = 30$ μm, $h = 19$ μm and A3: $d = 6$ μm, $l = 50$ μm, $h = 19$ μm). Sample A1 and A2 are around the optimal geometry for $h \sim 20$ μm and A3 is non-optimized. The micropillars were

etched on a silicon substrate (~600 μm thick) *via* deep reactive ion etching and a thin thermal

oxide (~50 nm) is grown to ensure that the surface is wetting. Samples with five different

wicking distances L (5-10 mm) were fabricated. A thin-film resistive heater was patterned on the

back side of each sample, which spans over the distance L. The sample was tilted 45 ° and dipped

into a reservoir filled with water in order to ensure that the liquid propagation is only *via*

wicking. We heated the sample in the ambient environment ($P = 1$ atm) and slowly increased the

heat flux. We obtained the dry-out heat flux when the liquid at $x = L$ started to recede. More

details about the sample and the experimental setup are described in Supporting Information. We

compared the measured $q_{dry\text{-}out}$ (Figure 8a) as a function of L with the model ($\theta_r = 15$ °). The

experimental data shows excellent agreement with the model.

Figure 8. (a) Experimental data and model of $q_{dry\text{-}out}$ *vs.* L on three wick geometries (A1:

$d = 7$ μm, $l = 20$ μm, $h = 20$ μm, A2: $d = 7$ μm, $l = 30$ μm, $h = 19$ μm and A3: $d = 6$ μm,

$l = 50$ μm, $h = 19$ μm) with different wicking length L. $\theta_r = 15$ °. (b) The dry-out heat flux $q_{dry\text{-}out}$

as a function of the wick surface length L as predicted by the model for two micropillar

geometries (B1: $d = 5$ μm, $l = 20$ μm, $h = 25$ μm and B2: $d = 5$ μm, $l = 10$ μm and $h = 25$ μm)

with $\theta_r = 15°$. Inset is a schematic showing a design that extends the reservoir region to the heat transfer surface by incorporating channels with minimal pressure drop from the main reservoir.

Finally, we discuss the effect of the wicking length L on $q_{dry\text{-}out}$, and show the importance of L, aside from the microstructure geometries, in capillary-pumped heat sink designs. Figure 8b shows $q_{dry\text{-}out}$ as a function of L based on our model for two micropillar geometries (Sample B1: $d = 5$ μm, $l = 20$ μm, $h = 25$ μm and B2: $d = 5$ μm, $l = 10$ μm and $h = 25$ μm). B1 is chosen close to the optimal micropillar geometries for $h = 25$ μm and B2 has non-optimized geometries (see Figure 6b). The dependence of $q_{dry\text{-}out}$ *vs.* L on a log-log scale appears linear which indicates a power law relationship between the two. In fact, the slopes in Figure 8b suggest that $q_{dry\text{-}out} \sim L^{-2}$. The physical reason behind this relationship is because $q_{dry\text{-}out} \times L$ scales with the total heat input Q to the surface, and $Q \propto \Gamma(x = 0) \propto P_{cap,max}/L$, where Γ is the liquid mass flow rate (equation (9)) and $P_{cap,max}$ is the maximum capillary pressure for a given micropillar geometry. Figure 8b indicates that, although the two geometries B1 and B2 lead to ~100% difference in $q_{dry\text{-}out}$ for the same L (see Figure 6c), $q_{dry\text{-}out}$ spans two orders of magnitude when L is varied from 1 mm to 10 mm. This suggests that: 1) It is possible to achieve a significant heat flux only over a small area, however this does not necessarily correspond to an optimized wick surface. 2) Achieving high heat fluxes as the wick surface scales up is difficult, since $q_{dry\text{-}out}$ quickly decreases with L^2. However it is possible to extend the reservoir region to the heat transfer surface by incorporating channels with minimal pressure drop from the main reservoir (inset of Figure 8b). This offers an opportunity to further enhance the dry-out heat flux by reducing the characteristic wicking length L while still increasing the total heat transfer surface length L_s (*i.e.*, $L_s > L$).

4. CONCLUSIONS

We have demonstrated a modeling framework to predict thin film evaporation in micropillar wick surfaces and we validated the model with experimental data. The model accurately captures the effect of the three-dimensional meniscus shape, which varies along the wicking direction, by solving the Young-Laplace equation. Dry-out heat flux for various micropillar structure geometries (height, pitch and diameter) in the length scale range of 1-100 μm with water as the working fluid was predicted and the optimal geometries to maximize the dry-out heat flux are suggested ($d/h \sim$ 0.4-0.6 and $l/d \sim$ 3). The dry-out heat flux $q_{dry\text{-}out}$ is very sensitive to the wicking length L and is governed by $q_{dry\text{-}out} \sim L^{-2}$. This suggests opportunities to enhance $q_{dry\text{-}out}$ by incorporating multiple reservoir channels inside the wicking area to reduce L. This work can be extended to other micropillar geometries such as squares but the non-uniformity of the contact angle around a pillar can result in a partial receding and partial pinning state, which needs further consideration. This work provides an important understanding of the heat transfer limitations of capillary-pumped thin-film evaporation on surfaces, and serves as a guideline for the design of high performance thermal management systems.

Associated Content

The Supporting Information is available free of charge on the ACS Publications website.

AUTHOR INFORMATION

Corresponding Author

* Corresponding Author: enwang@mit.edu

Notes: The authors declare no competing financial interest.

Author Contributions

REFERENCES

(1)   Pop, E. Energy Dissipation and Transport in Nanoscale Devices. *Nano Res.* **2010**, *3* (3), 147–169.
(2)   Mahajan, R.; Chiu, C.; Chrysler, G. Cooling a Microprocessor Chip. *Proc. IEEE* **2006**, *94* (8), 1476–1486.
(3)   Majumdar, A. Thermoelectric Devices: Helping Chips to Keep Their Cool. *Nat. Nanotechnol.* **2009**, *4* (4), 214–215.
(4)   Yang, F.; Dai, X.; Peles, Y.; Cheng, P.; Khan, J.; Li, C. Flow Boiling Phenomena in a Single Annular Flow Regime in Microchannels (I): Characterization of Flow Boiling Heat Transfer. *Int. J. Heat Mass Transf.* **2014**, *68*, 703–715.
(5)   Kandlikar, S. G.; Kuan, W. K.; Willistein, D. A.; Borrelli, J. Stabilization of Flow Boiling in Microchannels Using Pressure Drop Elements and Fabricated Nucleation Sites. *J. Heat Transf.* **2005**, *128* (4), 389–396.
(6)   Zhu, Y.; Antao, D. S.; Bian, D. W.; Zhang, T. J.; Wang, E. N. Reducing Instability and Enhancing Critical Heat Flux Using Integrated Micropillars in Two-Phase Microchannel Heat Sinks. In *2015 Transducers - 2015 18th International Conference on Solid-State Sensors, Actuators and Microsystems (TRANSDUCERS)*; 2015; pp 343–346.

(7) Kariya, H. A.; Peters, T. B.; Cleary, M.; Hanks, D. F.; Staats, W. L.; Brisson, J. G.; Wang, E. N. Development and Characterization of an Air-Cooled Loop Heat Pipe With a Wick in the Condenser. *J. Therm. Sci. Eng. Appl.* **2013**, *6* (1), 011010–011010.

(8) Weibel, J. A.; Garimella, S. V.; North, M. T. Characterization of Evaporation and Boiling from Sintered Powder Wicks Fed by Capillary Action. *Int. J. Heat Mass Transf.* **2010**, *53* (19–20), 4204–4215.

(9) Nam, Y.; Sharratt, S.; Byon, C.; Kim, S. J.; Ju, Y. S. Fabrication and Characterization of the Capillary Performance of Superhydrophilic Cu Micropost Arrays. *J. Microelectromechanical Syst.* **2010**, *19* (3), 581–588.

(10) Ranjan, R.; Patel, A.; Garimella, S. V.; Murthy, J. Y. Wicking and Thermal Characteristics of Micropillared Structures for Use in Passive Heat Spreaders. *Int. J. Heat Mass Transf.* **2012**, *55* (4), 586–596.

(11) Hale, R. S.; Ranjan, R.; Hidrovo, C. H. Capillary Flow through Rectangular Micropillar Arrays. *Int. J. Heat Mass Transf.* **2014**, *75*, 710–717.

(12) Xiao, R.; Enright, R.; Wang, E. N. Prediction and Optimization of Liquid Propagation in Micropillar Arrays. *Langmuir* **2010**, *26* (19), 15070–15075.

(13) Wang, Y. X.; Peterson, G. P. Analytical Model for Capillary Evaporation Limitation in Thin Porous Layers. *J. Thermophys. Heat Transf.* **2003**, *17* (2), 145–149.

(14) Ravi, S.; Horner, D.; Moghaddam, S. Monoporous Micropillar Wick Structures, I-Mass Transport Characteristics. *Appl. Therm. Eng.* **2014**, *73* (1), 1371–1377.

(15) Horner, D.; Ravi, S.; Moghaddam, S. Monoporous Micropillar Wick Structures, II-Optimization & Theoretical Limits. *Appl. Therm. Eng.* **2014**, *73* (1), 1378–1386.

(16) Brinkman, H. C. A Calculation of the Viscous Force Exerted by a Flowing Fluid on a Dense Swarm of Particles. *Appl. Sci. Res.* **1949**, *1* (1), 27–34.

(17) Du, S.-Y.; Zhao, Y.-H. Numerical Study of Conjugated Heat Transfer in Evaporating Thin-Films near the Contact Line. *Int. J. Heat Mass Transf.* **2012**, *55* (1–3), 61–68.

(18) Spivak, M. *A Comprehensive Introduction to Differential Geometry*, 3rd Edition.; Publish or Perish, 1999; Vol. 3.

(19) COMSOL Multiphysics. *User Manual, v. 5.0*; 2015.

(20) Kandlikar, S. G. A Theoretical Model to Predict Pool Boiling CHF Incorporating Effects of Contact Angle and Orientation. *J. Heat Transf.* **2001**, *123* (6), 1071–1079.

(21) Chu, K.-H.; Enright, R.; Wang, E. N. Structured Surfaces for Enhanced Pool Boiling Heat Transfer. *Appl. Phys. Lett.* **2012**, *100* (24), 241603.

(22) Raj, R.; Maroo, S. C.; Wang, E. N. Wettability of Graphene. *Nano Lett.* **2013**, *13* (4), 1509–1515.

(23) Weibel, J. A.; Kim, S. S.; Fisher, T. S.; Garimella, S. V. Carbon Nanotube Coatings for Enhanced Capillary-Fed Boiling from Porous Microstructures. *Nanoscale Microscale Thermophys. Eng.* **2012**, *16* (1), 1–17.

(24) Ćoso, D.; Srinivasan, V.; Lu, M.-C.; Chang, J.-Y.; Majumdar, A. Enhanced Heat Transfer in Biporous Wicks in the Thin Liquid Film Evaporation and Boiling Regimes. *J. Heat Transf.* **2012**, *134* (10), 101501–101501.

(25) Zhang, C.; Hong, F.; Cheng, P. Simulation of Liquid Thin Film Evaporation and Boiling on a Heated Hydrophilic Microstructured Surface by Lattice Boltzmann Method. *Int. J. Heat Mass Transf.* **2015**, *86*, 629–638.

TOC Graphic